RSC Advances

PAPER

View Article Online
View Journal | View Issue

Cite this: *RSC Adv.*, 2026, **16**, 24739

Influence of Si/Al ratio on NH_3-SCR activity over Cu-exchanged SAPO-34

Chundi Yan, * Zhaowei Wu, Meiyun Wang, Yue Wang, Qian Liu, Shujun Li and Yuxuan Zhang

Euro VII emission standards demand advanced deNO_x catalysts for lean-burn exhaust aftertreatment. Cu-SAPO-34 is a leading NH_3-SCR catalyst, yet its low-temperature activity and hydrothermal stability require improvement. This study establishes a quantitative structure–activity relationship linking framework Si/Al ratio to catalytic performance. SAPO-34 supports with varying Si/Al ratios (0.20–0.40) were synthesized, and corresponding Cu-SAPO-34 catalysts were prepared *via* ion exchange. Characterization (XRD, XRF, NH_3-TPD, H_2-TPR) revealed that optimal Si/Al ratio (0.361) yields highly dispersed Cu^{2+} ions and balanced Brønsted/Lewis acidity, achieving nearly 100% NO_x conversion at 235 °C and >90% NO_x conversion between 210–540 °C (550 ppm NO_x, 550 ppm NH_3, 6 vol% O_2, 10 vol% H_2O, GHSV = 120 000 h^{-1}). Critically, after severe hydrothermal aging (800 °C, 4 h, 10 vol% H_2O), this catalyst maintains >90% activity at 200–400 °C, demonstrating exceptional durability. Excessive silicon (Si/Al = 0.406) promotes Cu_xO_y cluster formation, degrading performance. These findings demonstrate that intermediate Si/Al ratios synergistically optimize activity and stability by balancing acidity, Cu dispersion, and structural integrity. This work provides actionable design principles for developing robust Cu-SAPO-34 catalysts meeting stringent Euro VII standards.

Received 8th March 2026
Accepted 4th May 2026

DOI: 10.1039/d6ra01986b

rsc.li/rsc-advances

1. Introduction

Nitrogen oxides (NO_x), inevitable byproducts of high-temperature combustion of fossil fuels, contribute to photochemical smog, acid deposition, and adverse effects on human respiratory and cardiovascular systems.[1–3] Diesel vehicles, gas turbines, and industrial boilers, characterized by their "high-temperature lean-burn" operational conditions, represent major sources of NO_x emissions and constitute the primary targets of stringent emission regulations worldwide.[4] The Euro VII standard has tightened the NO_x limit for diesel vehicles to 80 mg km^{-1} (NEDC), with an anticipated further reduction of 35–56% in total NO_x emissions from passenger cars, vans, and heavy-duty trucks compared to Euro VI by 2035.[5]

Selective catalytic reduction utilizing ammonia as the reductant (NH_3-SCR) has emerged as the predominant technology for deep deNO_x under lean-burn conditions, owing to its high efficiency, economic viability, and technological maturity.[6] Since the beginning of the twenty-first century, copper-based chabazite (Cu-CHA) catalysts have risen to prominence, with small-pore catalysts such as Cu-SAPO-34 and Cu-SSZ-13 being discovered and commercialized by researchers from BASF and Johnson Matthey.[7] However, the synthesis of SSZ-13 relies on expensive and environmentally persistent *N*,*N*,*N*-trimethyl-1-adamantylammonium hydroxide (TMAdaOH). The high cost of this template greatly increases production expenses and severely restricts its large-scale application.[8,9] In contrast, SAPO-34 can be synthesized using benign and cost-effective organic amines such as triethylamine, morpholine, and diethylamine as structure-directing agents, offering significant advantages in cost control and green manufacturing.[10,11] Nevertheless, Cu-SAPO-34 still faces challenges of insufficient low-temperature activity and structural vulnerability under severe hydrothermal conditions.[12,13] Consequently, there is an urgent need to achieve rational design and optimization of catalysts based on the correlation between microscopic structure and intrinsic catalytic properties.

The framework Si/Al ratio of SAPO-34 serves as a critical parameter governing its acidity, Cu^{2+} ion-exchange capacity, and structural stability. Yu *et al.*[14] investigated Cu/SAPO-34 catalysts across a SiO_2/Al_2O_3 ratio range of 0.2 to 1.4 and found that while increased acidity enhances low-temperature activity, the formation of Si islands at higher Si loadings limits the linear correlation between Si content and acidity, thereby influencing the trade-off between SCR activity and NH_3 oxidation. However, this study primarily focused on kinetic aspects and NH_3 oxidation competition at low Cu loadings, failing to establish an optimal Si/Al ratio for balanced performance or to evaluate the catalysts under severe hydrothermal aging conditions. Similarly, Li *et al.*[15] demonstrated that within the SiO_2/Al_2O_3 ratio range of 0.4–0.8, increasing the silicon

School of Petroleum and Chemical Engineering, Dongying Vocational College, Dongying 257000, Shandong, China. E-mail: cindydicp@163.com

content enhances the crystallinity and total acidity of Cu-SAPO-34, resulting in superior C_3H_6-SCR performance at a ratio of 0.8. Nevertheless, this finding is specific to hydrocarbon-based reduction (C_3H_6-SCR), which operates under different mechanistic constraints compared to the NH_3-SCR systems required for modern diesel applications, and lacks the quantitative durability data essential for Euro VII compliance. The durability aspect has been partially addressed by Xiang *et al.*,[16] who found that high-silica samples (H–Si) are prone to framework hydrolysis (Si–O–Al bond cleavage) under low-temperature steam conditions (50 °C), whereas low-silica samples (L–Si) exhibit superior low-temperature hydrothermal stability due to fewer bridging hydroxyl groups. In contrast, Wang *et al.*[17] correlated silicon content with acidity and Cu^{2+} species using commercially sourced or conventionally prepared samples, concluding that higher Si content generally benefits low-temperature activity. Previous studies have explored the influence of silicon content, yet they often focus on isolated aspects of performance or specific conditions, lacking the precise synthetic control to identify the subtle trade-off between Brønsted acidity and Cu speciation. Consequently, for Cu-SAPO-34 catalysts applied in NH_3-SCR, a quantitative structure–activity relationship that simultaneously links framework Si content, Brønsted/Lewis acid balance, copper dispersion, and hydrothermal durability remains to be established.

In this context, the present study employs hydrothermal crystallization using inexpensive triethylamine as the sole template, adopting a single-variable strategy to precisely control the initial gel Si/Al ratio (0.2–0.4) for the preparation of a series of SAPO-34 supports with tunable crystallinity and varying framework silicon substitution degrees. Copper active centers were subsequently introduced under rigorously identical ion-exchange conditions. Through systematic characterization using XRD, NH_3-TPD, H_2-TPR, ICP-OES, and XRF techniques, the effects of Si/Al ratio on acid site distribution, Cu^{2+} exchange capacity, chemical state of Cu species, and high-temperature hydrothermal stability were elucidated. Subsequently, these intrinsic properties were quantitatively correlated with standard SCR reaction activity. We propose a quantitative framework linking acidity, Cu dispersion, and hydrothermal durability within the investigated Si/Al range, offering insights for the design of high-performance deNO_x catalysts.

2. Catalyst preparation

2.1 Hydrothermal synthesis of SAPO-34 molecular sieves

SAPO-34 molecular sieves were synthesized *via* hydrothermal crystallization using triethylamine (TEA) as the sole structure-directing agent.[18] Reaction mixtures with target Si/Al atomic ratios (x = 0.1–0.5) were prepared according to the following procedure: 24.9 g of 85 wt% orthophosphoric acid, 92 mL of deionized water, 14.4 g of 70 wt% pseudoboehmite, 36.4 g of triethylamine, and the requisite quantity of 30–31 wt% silica sol (calculated based on the target Si/Al ratio) were sequentially added to a beaker. The mixture was vigorously stirred at ambient temperature for 2 h to obtain a homogeneous gel. The gel was subsequently transferred to a Teflon-lined stainless-steel autoclave, sealed, and subjected to static aging at 110 °C for 12 h, followed by crystallization at 200 °C for 48 h. After natural cooling to ambient temperature, the supernatant was decanted, and the solid product was ground, thoroughly washed with deionized water until the filtrate reached neutral pH, dried at 110 °C for 12 h, and finally calcined in static air at 550 °C for 8 h to completely remove the organic template. The resulting samples were designated as SAPO-34-x (x = 0.1, 0.2, 0.3, 0.4, 0.5) according to their Si/Al ratios. It should be particularly noted that at x = 0.1 and 0.5, insufficient quantities of phase-pure SAPO-34 products were obtained; consequently, subsequent characterization was conducted exclusively on qualified samples synthesized under x = 0.2, 0.3, and 0.4 conditions.

2.2 Ion-exchange preparation of Cu-SAPO-34 catalysts

Cu-exchanged SAPO-34 catalysts were synthesized *via* a two-step ion-exchange method. In the first step, NH_4^+ pre-exchange was performed by dispersing SAPO-34-x molecular sieves in a 3.24 mol L^{-1} NH_4Cl aqueous solution at a solid-to-liquid ratio of 1 g : 10 mL, followed by stirring at 80 °C for 2 h; the resulting products were thoroughly washed with deionized water until the absence of Cl^- in the filtrate was confirmed by $AgNO_3$ titration and subsequently dried at 110 °C. In the second step, Cu^{2+} exchange was conducted by dispersing the as-obtained NH_4^+-exchanged intermediates in a 0.025 mol L^{-1} $Cu(NO_3)_2$ aqueous solution at a solid-to-liquid ratio of 1 g : 100 mL with stirring at 80 °C for 4 h; after exhaustive washing with deionized water and drying at 110 °C, the samples were calcined in static air at 550 °C for 5 h. The resulting catalysts were designated as Cu-SAPO-34-x (x = 0.2, 0.3, 0.4), consistent with the nomenclature of their parent SAPO-34-x precursors.

2.3 Characterization

2.3.1 X-ray Diffraction (XRD). Phase identification was performed on a Rigaku RINT D/MAX-2500PC diffractometer (Rigaku Corp., Tokyo, Japan) using Cu Kα radiation (λ = 0.15406 nm, Kα_1) operated at 40 kV and 200 mA. Data were collected over a 2θ range of 5–50° at a scan rate of 5° min^{-1} with a step size of 0.02°. Phase identification was accomplished using MDI Jade 6.0 software in conjunction with the ICDD PDF-4+ database.

2.3.2 X-ray fluorescence spectroscopy (XRF). Elemental composition analysis was performed on a PANalytical Magix PRO PW2404 wavelength-dispersive X-ray fluorescence spectrometer (WDXRF) equipped with a Rh target X-ray tube. Samples were prepared as fused beads, and quantitative analysis was conducted using the fundamental parameters method with calibration against certified reference materials.

2.3.3 Inductively coupled plasma optical emission spectroscopy (ICP-OES). Copper content was determined using a Shimadzu ICPS-8100 ICP-OES spectrometer (Shimadzu Corp., Kyoto, Japan). Samples were digested with a mixture of concentrated HNO_3 and HF (3 : 1 v/v) in PTFE vessels, subsequently evaporated to near dryness, redissolved in 2% HNO_3, and diluted to a final concentration of 10 mg L^{-1} for analysis.

The Cu 324.752 nm emission line was monitored using yttrium as an internal standard.

2.3.4 NH_3 temperature-programmed desorption (NH_3-TPD). Acidity characterization was conducted on a Quantachrome ChemBET 3000 chemisorption analyzer (Quantachrome Instruments, Boynton Beach, FL, USA). Approximately 200 mg of sample was loaded into a quartz U-tube reactor. The sample was pretreated by purging with He (30 mL min^{-1}) at 400 °C for 30 min, cooled to 100 °C, and then saturated with 0.5% NH_3/N_2 (v/v, 30 mL min^{-1}) for 30 min. Physisorbed NH_3 was subsequently removed by purging with He (30 mL min^{-1}) at 100 °C for 30 min. After baseline stabilization, the temperature was ramped to 700 °C at 10 °C min^{-1} under He flow (30 mL min^{-1}), with desorbed NH_3 monitored by a thermal conductivity detector (TCD). Quantitative calibration was performed using a calibrated loop injection of pure NH_3.

2.3.5 H_2 temperature-programmed reduction (H_2-TPR). Reducibility measurements were performed on the same Quantachrome ChemBET 3000 analyzer. The sample (*ca.* 100 mg) was pretreated by purging with Ar (30 mL min^{-1}) at 500 °C for 30 min and cooled to room temperature. After switching to 10% H_2/Ar (v/v, 30 mL min^{-1}) and allowing baseline stabilization for 30 min, the temperature was increased to 950 °C at 10 °C min^{-1}. Hydrogen consumption was recorded by TCD and quantified using CuO as a calibration standard.

2.4 Catalytic performance evaluation

NH_3-SCR activity tests were conducted in a fixed-bed quartz tubular reactor with an internal diameter of 10 mm. The catalysts were pelletized, crushed, and sieved to 40–60 mesh, with a catalyst loading of 0.6000 g (approximately 0.75 mL), resulting in a bed height-to-diameter ratio of approximately 1.0. The simulated flue gas composition consisted of 550 ppm NO_x (NO/NO_2 > 95/5), 550 ppm NH_3, 6 vol% O_2, 10 vol% H_2O, balanced with N_2, at a gas hourly space velocity (GHSV) of 120 000 h^{-1}. The reactor effluent was passed through a cold trap for water removal prior to online analysis using a Thermo Nicolet 6700 Fourier-transform infrared spectrometer (FTIR, USA) equipped with a KBr beam splitter and a DTGS detector. The spectral resolution was 0.1 cm^{-1}, with 32 scans for background and 4 scans for sample acquisition. NO_x conversion was calculated according to eqn (1):

$$NO_x\ \text{conversion}(\%) = \frac{\Phi(NO + NO_2)_{inlet} - \Phi(NO + NO_2)_{outlet}}{\Phi(NO + NO_2)_{inlet}} \quad (1)$$

In automotive exhaust aftertreatment systems, the SCR catalyst is generally arranged downstream of the diesel particulate filter (DPF). During active DPF regeneration, the exhaust temperature at the upstream of SCR can rapidly rise to 750–800 °C, accompanied by a high concentration of water vapor (5–10 vol%) in actual diesel exhaust, causing severe hydrothermal shock and long-term aging damage to the SCR catalyst.[7,19,20] Accordingly, the hydrothermal aging test in this work was reasonably designed to simulate the actual service condition: the catalyst was treated *in situ* in a reaction tube, heated to 800 °C and held for 4 h under an air atmosphere containing 10 vol% H_2O. The gas flow rate was kept consistent with that used in the catalytic activity evaluation to ensure the accuracy and credibility of the aging simulation.

3. Results and discussion

3.1 Influence of initial gel Si/Al ratio on the crystal structure of SAPO-34

Syntheses demonstrated that the initial gel Si/Al ratio profoundly influences phase formation. At Si/Al = 0.1, only trace amounts of amorphous solid precipitated; at Si/Al = 0.2–0.4, approximately 10 g of crystalline product was obtained; while at Si/Al = 0.5, gelation occurred, preventing phase-pure SAPO-34 formation. These contrasting outcomes may be attributed to pH variations induced by silica sol modulation: insufficient silica at Si/Al = 0.1 and excessive silica at Si/Al = 0.5 both deviate from optimal gel chemistry, disrupting SAPO-34 crystallization.[21] We hypothesize that these extreme ratios shifted the gel pH outside the thermodynamic stability field of SAPO-34. Consequently, characterization was restricted to samples with initial gel Si/Al ratios of 0.2, 0.3, and 0.4.

Fig. 1 displays the X-ray diffraction (XRD) patterns of SAPO-34 molecular sieves synthesized with varying initial Si/Al gel ratios (x = 0.2, 0.3, and 0.4). All samples exhibited characteristic diffraction peaks corresponding to the chabazite (CHA) structure, which were in excellent agreement with the standard PDF card (No. 87-1527), and no peaks attributable to crystalline impurities were detected.[18]

These results confirm the successful synthesis of phase-pure SAPO-34 molecular sieves within the gel ratio range of $0.2 \le x \le 0.4$. Quantitative analysis by X-ray fluorescence (XRF) spectrometry (Table 1) revealed that as the gel Si/Al ratio increased from 0.2 to 0.4, the measured Si/Al ratio in the solid products rose correspondingly from 0.299 to 0.406, confirming the progressive incorporation of silicon into the framework. However, the extent of this increase was less pronounced than that of the gel composition, suggesting that the substitution of

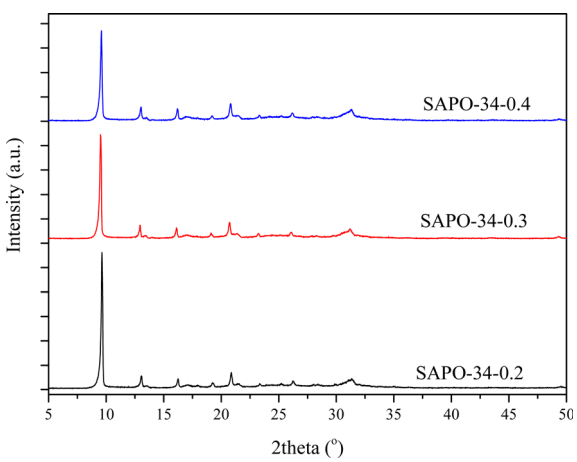

Fig. 1 XRD patterns of SAPO-34-x with different Si/Al ratios (x = 0.2, 0.3, 0.4).

Table 1 Synthesis parameters of SAPO-34 molecular sieves and characterization results by XRF and XRD

Initial Si/Al molar ratio in the gel	Synthesized molecular sieve designation	XRF analysis				XRD analysis		
		Si/Al atomic ratio	Si/(Al + P + Si)	Al/(Al + P + Si)	P/(Al + P + Si)	Signal-to-noise ratio	Crystall-inity degree	Crystall-ite size
0.2	SAPO-34-0.2	0.299	0.111	0.372	0.516	40.3	82.97	785
0.3	SAPO-34-0.3	0.361	0.133	0.368	0.500	35.2	92.73	547
0.4	SAPO-34-0.4	0.406	0.146	0.359	0.495	32.6	88.80	543

silicon is governed by a combination of thermodynamic and crystal growth kinetic factors. Notably, the relative crystallinity exhibited a volcano-type dependence on silicon content. As schematically illustrated in Fig. 2, two silicon substitution mechanisms (SM2 and SM3) exist in the SAPO-34 framework.[17,22,23] When the gel ratio increased from 0.2 to 0.3, crystallinity improved markedly from 82.97% to 92.73%, predominantly driven by the SM2 substitution mechanism,[22,23] in which silicon substitutes for phosphorus, thereby stabilizing the framework charge. In contrast, a further increase to a gel ratio of 0.4 led to a decrease in crystallinity to 88.80%, accompanied by a reduction in the XRD signal-to-noise ratio from 40.3 to 32.6. This decline implies that excessive silicon promotes the dominance of the SM3 substitution mechanism,[17,22] involving the coupled substitution of silicon for adjacent aluminum and phosphorus atoms, potentially resulting in the formation of silicon islands and localized structural disorder. Moreover, the average crystallite size decreased substantially with increasing gel ratio (from 785 nm to 543 nm), attributable to enhanced nucleation and suppressed crystal growth under silicon-rich conditions. The convergence of crystallite sizes between SAPO-34-0.3 and SAPO-34-0.4 suggests that a dynamic equilibrium between nucleation and growth is established once the Si/Al ratio exceeds 0.3. These structural variations are expected to exert a significant influence on the acidity and catalytic performance of the resulting molecular sieves.

3.2 Influence of Si/Al ratio on the Acidity of SAPO-34 and Cu-SAPO-34 catalysts

Fig. 3 presents the NH_3-TPD profiles of SAPO-34-x ($x = 0.2, 0.3, 0.4$) with varying Si/Al ratios. All samples exhibit characteristic bimodal desorption features: the low-temperature desorption (LTD) peak at 200–300 °C is attributed to NH_3 desorption from weak Lewis acid sites and physisorbed NH_3, whereas the high-temperature desorption (HTD) peak at 450–550 °C corresponds to NH_3 desorption from strong Brønsted acid sites.[18,24,25] As the framework Si/Al ratio increases from 0.299 to 0.406, the LTD peak temperature rises from 214 °C to 246 °C, and the HTD peak temperature increases from 450 °C to 494 °C. The concurrent increase in peak temperatures and areas indicates a synergistic enhancement of acid strength and acid amount with increasing silicon content. This phenomenon can be rationalized by silicon substitution mechanisms: at low Si/Al ratios, Si predominantly substitutes isolated P sites *via* the SM2 mechanism, forming Si(4Al) coordination environments that generate isolated Brønsted acid sites of moderate strength; at high Si/Al ratios, the SM3 mechanism prevails, facilitating silicon island formation and creating silicon-rich coordination environments such as Si(0Al) and Si(1Al), thereby enhancing acid strength and density. Additionally, the smaller crystallite size of SAPO-34-0.4 (543 nm) significantly shortens the intracrystalline diffusion path length. According to the Maxwell–Stefan (M–S) diffusion theory and the concept of the Thiele modulus, a shorter path length reduces the Thiele modulus,[26] thereby alleviating intracrystalline diffusion limitations and potentially improving the effective accessibility of reactants like NH_3 to the internal active sites. This theoretical prediction is corroborated by the enhanced NH_3-TPD signal intensity observed in our sample, which suggests a higher utilization efficiency of the micropore volume compared to bulkier crystals.[27]

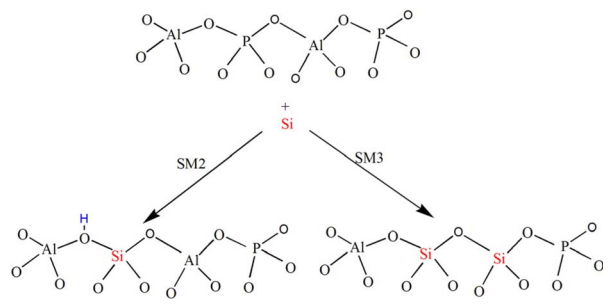

Fig. 2 Scheme of the SM2 and SM3 mechanisms for Si substitution into the SAPO-34 framework. The oxidation states of Al, P, and Si are +III, +V, and +IV, respectively, as commonly adopted in aluminophosphate-based zeolites.

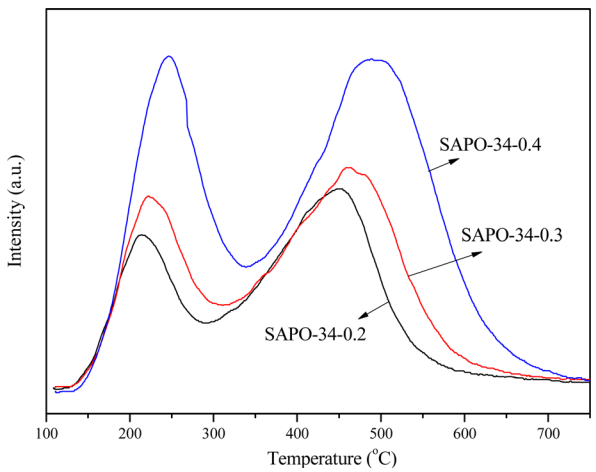

Fig. 3 NH_3-TPD profiles of SAPO-34-x with different Si/Al ratios ($x = 0.2, 0.3, 0.4$).

The acidic characteristics of these phase-pure SAPO-34 samples provide a fundamental basis for understanding the evolution of acidity upon Cu ion exchange. Fig. 4 displays the NH_3-TPD profiles of Cu-modified samples. All samples exhibit two NH_3 desorption peaks at approximately 210 °C (LTD) and 400 °C (HTD). According to the literature,[28] the LTD peak is assigned to NH_3 desorption from weak Lewis acid sites associated with Cu species, P–OH groups, and extra-framework aluminum species, while the HTD peak corresponds to Brønsted acid sites and strong Lewis acid sites related to Cu^{2+}.[14,16,18] The introduction of Cu results in a significant decrease in HTD peak temperature (*e.g.*, from 470 °C for SAPO-34-0.3 to 352 °C for Cu-SAPO-34-0.3), indicating that Cu^{2+} can modulate the acid strength distribution. The Cu-SAPO-34 catalysts with different Si/Al ratios follow the same order in both LTD and HTD peak positions: Cu-SAPO-34-0.3 (support Si/Al = 0.361) shows the lowest LTD and HTD peak temperatures (210 °C and 352 °C), followed by Cu-SAPO-34-0.2 (215 °C and 362 °C), and Cu-SAPO-34-0.4 (227 °C and 373 °C). Notably, Cu-SAPO-34-0.3 exhibits the lowest HTD peak temperature with the largest peak area, suggesting the formation of abundant and moderately strong Cu^{2+}-associated Lewis acid sites in this sample, which provides a crucial acidic structural foundation for its superior low-temperature activity in NH_3-SCR reactions. These variations may be associated with differences in Cu loading and chemical states on supports with different Si/Al ratios.

3.3 Influence of Si/Al ratio on copper reducibility and loading

To gain deep insights into the influence of the SAPO-34 framework Si/Al ratio on the existing morphology and siting of Cu species after ion exchange, H_2-TPR technique was employed to systematically characterize the reduction behavior of Cu-SAPO-34 samples with varying Si/Al ratios, and the results are presented in Fig. 5. The H_2-TPR profiles of Cu-SAPO-34-0.2 and Cu-SAPO-34-0.3 exhibit similar features, both displaying

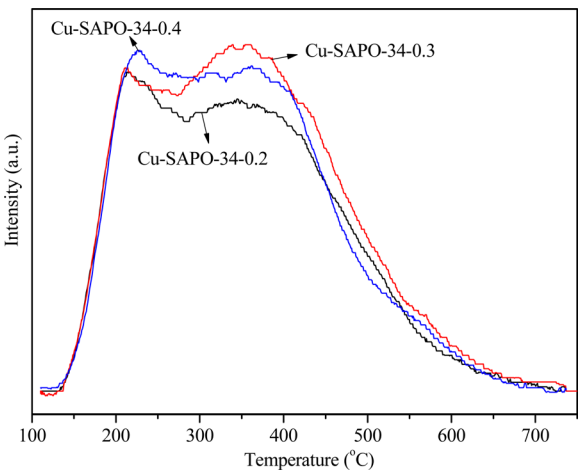

Fig. 4 NH_3-TPD profiles of Cu-SAPO-34-*x* with different Si/Al ratios (*x* = 0.2, 0.3, 0.4).

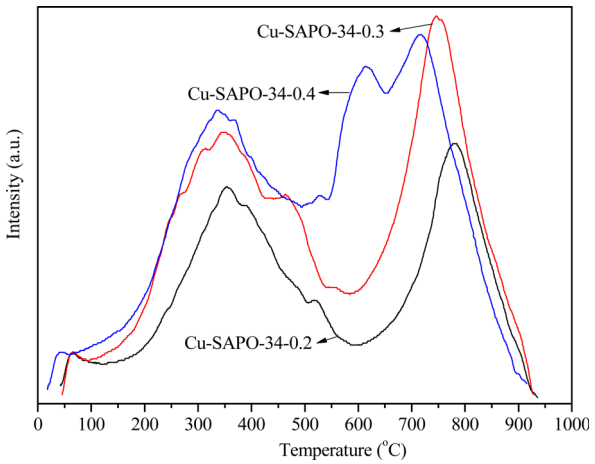

Fig. 5 H_2-TPR profiles of Cu-SAPO-34-*x* with different Si/Al ratios (*x* = 0.2, 0.3, 0.4).

two characteristic reduction peaks at approximately 350 °C and 800 °C. Specifically, the low-temperature reduction peak at ~350 °C corresponds to the one-step reduction of isolated Cu^{2+} ions located at the six-membered ring site I to Cu^+, whereas the high-temperature reduction peak at ~800 °C is attributed to the subsequent reduction of the resulting Cu^+ to Cu^0.[18,29,30] As the Si/Al ratio increases from 0.299 to 0.361, the integrated areas of both low- and high-temperature reduction peaks increase concomitantly, which correlates well with the Cu loading determined by ICP-OES rising from 1.59 wt% to 2.37 wt%. This observation indicates that an appropriate Si/Al ratio can effectively facilitate Cu^{2+} ion exchange and favor the formation of highly dispersed active sites. Nevertheless, upon further increasing the Si/Al ratio to 0.406 (Cu-SAPO-34-0.4), an additional medium-temperature reduction peak emerges at ~630 °C in its H_2-TPR profile, which can be assigned to the reduction of Cu_xO_y clusters.[31–33] Simultaneously, the high-temperature reduction peak shifts from 800 °C to ~735 °C, implying that a fraction of Cu^{2+} ions may preferentially occupy weakly interacting sites such as site IV at the eight-membered ring window of the zeolite framework.[18,30] This excessive Si/Al ratio-induced migration of Cu species siting and the formation of binuclear/oligomeric Cu species may lead to a decreased dispersion of active sites, thereby exerting adverse effects on low-temperature SCR activity and posing a potential threat to high-temperature hydrothermal stability.

3.4 Influence of Si/Al ratio on SCR activity and high-temperature hydrothermal stability of Cu-SAPO-34 catalysts

To elucidate how the initial Si/Al ratio regulates the catalytic performance and hydrothermal stability of Cu-SAPO-34 in NH_3-SCR, NO_x conversions were measured for both fresh and hydrothermally aged samples (Fig. 6). The catalytic activity of fresh samples (Fig. 6, solid symbols) revealed that Cu-SAPO-34-0.3 (Si/Al = 0.361) exhibited the optimal catalytic performance among all samples, achieving nearly 100% NO_x conversion at 235 °C and maintaining >90% conversion over a broad

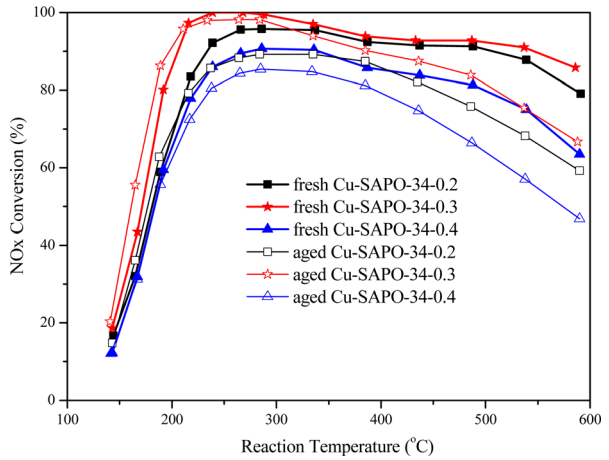

Fig. 6 Effect of Si/Al ratio on NH_3-SCR activity and hydrothermal stability of Cu-SAPO-34-x catalysts (x = 0.2, 0.3, 0.4).

temperature window of 210–540 °C. Compared with benchmark Cu-SSZ-13 and Cu-SAPO-34 catalysts reported in the literature,[7,34,35] our optimized Cu-SAPO-34 exhibits a comparable fresh activity window (*e.g.*, a Cu/SSZ-13 catalyst maintains >90% NO conversion from 200 °C to 550 °C).[34] By comparison, Cu-SAPO-34-0.2 and Cu-SAPO-34-0.4 achieved NO_x conversions of approximately 90% and 85% at 235 °C, respectively; notably, the latter exhibited the lowest catalytic activity across the entire temperature range, declining to merely ~63% at 590 °C. The superior low-temperature activity of Cu-SAPO-34-0.3 can be attributed to its relatively high crystallinity (92.73%), appropriate acidity, and optimal Cu^{2+} exchange capacity (2.37 wt%), which synergistically facilitated the formation of isolated Cu^{2+} active sites.[18,36] Conversely, the activity decline observed at elevated temperatures was primarily associated with non-selective NH_3 oxidation and N_2O formation, involving structural evolution processes such as CuO_x species aggregation and Brønsted acid site dehydroxylation.

Following hydrothermal aging (Fig. 6, open symbols), all catalyst samples exhibited varying degrees of deactivation; however, the extent of activity degradation and the temperature-dependent activity profiles differed substantially, further underscoring the critical regulatory role of the initial Si/Al ratio in hydrothermal stability. Notably, Cu-SAPO-34-0.3 (Si/Al = 0.361) demonstrated the highest hydrothermal durability, maintaining NO_x conversions above 90% within the temperature range of 200–400 °C; Cu-SAPO-34-0.2 ranked second, with its catalytic activity peaking at 280–340 °C and reaching a maximum conversion of approximately 90%; whereas Cu-SAPO-34-0.4 (Si/Al = 0.406) suffered the most severe deactivation, with the maximum conversion never exceeding 85% across the entire temperature range and dropping to merely ~47% at 590 °C. This disparity in stability can be attributed to the balanced framework charge distribution resulting from the moderate Si/Al ratio (0.361), which effectively suppressed framework dealumination and Cu species migration/agglomeration during hydrothermal aging.[18,37]

4. Conclusions

This study reports the successful synthesis of a series of high-crystallinity SAPO-34 molecular sieves with varying framework Si/Al ratios (0.299–0.406) achieved by modulating the incorporation of silica sol in the initial gel. The corresponding Cu-SAPO-34 catalysts were subsequently prepared using an identical ion-exchange procedure. This approach systematically elucidates the regulatory mechanisms of the initial gel Si/Al ratio on support structure, acidity, Cu species siting, and NH_3-SCR catalytic performance. Phase-pure SAPO-34 was synthesized within a Si/Al range of 0.20–0.40 using triethylamine as the sole template. An optimal Si/Al ratio of 0.361 endows the catalyst with a high density of strong Brønsted acid sites and highly dispersed isolated Cu^{2+} species, achieving nearly 100% NO_x conversion at 235 °C, maintaining over 90% conversion across the temperature range of 210–540 °C, and retaining above 90% activity between 200 and 400 °C after hydrothermal aging at 800 °C. It should be emphasized that the optimal NH_3-SCR activity of Cu-SAPO-34 prepared with a Si/Al ratio of 0.361 is system-dependent. This optimal value is strictly constrained by factors such as synthesis parameters, pretreatment procedures, ion-exchange conditions, and copper loading during the actual preparation process. Nevertheless, the regulatory effect of the framework Si/Al ratio on the structural properties and catalytic behavior of Cu-SAPO-34 is generally applicable to its deNO_x system. This superior performance originates from the synergistic effects of isolated Cu^{2+} ions located at six-membered ring sites, moderate acidity, and a balanced framework composition. In contrast, a low Si/Al ratio (0.299) limits the density of active sites, while a high Si/Al ratio (0.406) induces the formation of Cu_xO_y clusters due to framework charge imbalance, thereby compromising catalytic activity and stability. These quantitative structure–activity relationships provide guidelines for the rational design of Cu-SAPO-34 deNO_x catalysts capable of meeting stringent emission standards, including Euro VII.

Author contributions

Chundi Yan: conceptualization, investigation, methodology, writing – original draft, writing – review & editing, funding acquisition; Zhaowei Wu: investigation, writing – review & editing; Meiyun Wang: investigation, writing – review & editing, formal analysis; Yue Wang: investigation, validation; Qian Liu: investigation, resources; Shujun Li: resources, investigation; Yuxuan Zhang: investigation, formal analysis. All authors have read and agreed to the published version of the manuscript.

Conflicts of interest

There are no conflicts to declare.

Data availability

The authors confirm that the data supporting the findings of this study are available in the article.

Acknowledgements

This work was financially supported by the Young Scientists Fund of the Shandong Provincial Natural Science Foundation (Grant No. ZR2024QB230). The authors are also grateful to the Center for Energy and Environmental Engineering Research, Dalian Institute of Chemical Physics, Chinese Academy of Sciences, for providing experimental facilities and technical assistance.

References

1 World Health Organization (WHO), *WHO global air quality guidelines: particulate matter (PM2.5 and PM10), ozone, nitrogen dioxide, sulfur dioxide and carbon monoxide*, World Health Organization, Geneva, 2021, https://www.who.int/publications/i/item/9789240034228.

2 S. Li, G. Li, L. He, H. Wang, L. Ji, J. Wang, W. Chen, Y. Kang and H. Yin, *Transp. Res., Part D Transp. Environ.*, 2025, **146**, 104875, DOI: 10.1016/j.trd.2025.104875.

3 S. Lu, C. Shen, M. Liu, J. Zhang, M. Fang, F. Wang, Q. Li, C. Li and J. Zhang, *Results Eng.*, 2025, **25**, 103677, DOI: 10.1016/j.rineng.2024.103677.

4 J. Chen, W. Huang, S. Bao, W. Zhang, T. Liang, S. Zheng, L. Yi, L. Guo and X. Wu, *RSC Adv.*, 2022, **12**, 27746, DOI: 10.1039/d2ra05107a.

5 J. Dornoff and F. Rodríguez, *Euro 7: The new emission standard for light- and heavy-duty vehicles in the European Union*, International Council on Clean Transportation, 2024, https://theicct.org/wp-content/uploads/2024/03/ID-116-%E2%80%93-Euro-7-standard_final.pdf.

6 Z. Cui, R. Guo, J. Lv, X. Shi and W. Pan, Recent progress on low-temperature selective catalytic reduction of NOx by NH3 based on MOF-derived materials: a review, *Nanoscale*, 2025, **17**, 26594–26620, DOI: 10.1039/D5NR03710G.

7 D. Wang, Y. Jangjou, Y. Liu, M. K. Sharma, J. Luo, J. Li, K. Kamasamudram and W. S. Epling, *Appl. Catal. B Environ.*, 2015, **165**, 438–445, DOI: 10.1016/j.apcatb.2014.10.020.

8 L. Wang, D. Zhu, J. Wang, W. Cui, J. Han, B. Li, D. Fan, P. Tian and Z. Liu, *J. Mater. Chem. A*, 2021, **9**(27), 15238–15245, DOI: 10.1039/D1TA01452H.

9 W. Liu, J. Zhang, M. Dong, Z. Ding, Q. Wang, F. Ning, Q. He, Y. Chen, Z. Zhao, Z. Li and C. Liu, *Sep. Purif. Technol.*, 2025, **354**, 129201, DOI: 10.1016/j.seppur.2024.129201.

10 M. Nazari, *J. Chem. Rev.*, 2023, **5**(4), 394–415, DOI: 10.48309/JCR.2023.408079.1237.

11 M. Jabłońska, K. Góra-Marek, M. F. Lukman, K. Tarach, M. Bertmer, R. Denecke, D. Poppitz, K. Marcinowski, A. Pöppl and R. Gläser, *Catal. Sci. Technol.*, 2022, **12**, 6660, DOI: 10.1039/d2cy01548j.

12 J. Hou, C. Zhong, C. Yin, R. Liu, L. Wang and Z. Zhao, *Sep. Purif. Technol.*, 2025, **377**, 134197, DOI: 10.1016/j.seppur.2025.134197.

13 J. Luo, H. Xu, X. Liang, S. Wu, Z. Liu, Y. Tie, M. Li and D. Yang, *Res. Chem. Intermed.*, 2023, **49**, 2321–2357, DOI: 10.1007/s11164-022-04938-9.

14 Y. Tie, J. Wang, M. Shen and W. Li, *Catal. Sci. Technol.*, 2013, **3**, 3234–3241, DOI: 10.1039/c3cy00453h.

15 X. Li, H. Yan, J. Lv, L. Bai and F. Jin, *Chem. Ind. Eng.*, 2017, **34**(3), 8–12, DOI: 10.13353/j.issn.1004.9533.20151088.

16 X. Xiang, P. Wu, Y. Cao, L. Cao, Q. Wang, S. Xu, P. Tian and Z. Liu, *Chin. J. Catal.*, 2017, **38**, 918–927, DOI: 10.1016/S1872-2067(17)62836-5.

17 J. Wang, T. Yu, X. Wang, G. Qi, J. Xue, M. Shen and W. Li, *Appl. Catal. B Environ.*, 2012, **127**, 137–147, DOI: 10.1016/j.apcatb.2012.08.016.

18 C. Yan, H. Cheng, Z. Yuan and S. Wang, *Environ. Technol.*, 2015, **36**, 169–177, DOI: 10.1080/09593330.2014.941017.

19 S. J. Schmieg, S. H. Oh, C. H. Kim, D. B. Brown, J. H. Lee, C. H. F. Peden and D. H. Kim, *Catal. Today*, 2012, **184**, 252–261, DOI: 10.1016/j.cattod.2011.10.034.

20 J. H. Kwak, D. Tran, S. D. Burton, J. Szanyi, J. H. Lee and C. H. F. Peden, *J. Catal.*, 2012, **287**, 203–209, DOI: 10.1016/j.jcat.2011.12.025.

21 Y. Duan, H. Dai, L.-S. Wang, M. Zhang, L.-M. Wu and G. Ouyang, *J. Solid State Chem.*, 2022, **309**, 123011, DOI: 10.1016/j.jssc.2022.123011.

22 G. Sastre, D. W. Lewis and C. R. A. Catlow, *J. Mol. Catal. A:Chem.*, 1997, **119**(1–3), 349–356, DOI: 10.1016/S1381-1169(96)00498-0.

23 K. Kvande, D. K. Pappas, M. Dyballa, C. Buono, M. Signorile, E. Borfecchia, K. A. Lomachenko, B. Arstad, S. Bordiga, G. Berlier, U. Olsbye, P. Beato and S. Svelle, *Catalysts*, 2020, **10**(2), 193, DOI: 10.3390/catal10020191.

24 Y. Duan, J. Wang, T. Yu, M. Shen and J. Wang, *RSC Adv.*, 2015, **5**, 14103, DOI: 10.1039/c4ra13984d.

25 S. Lu, Y. Xue, F. Meng, M. Liu, T. Hou, Y. Luo, L. Liu, Y. An, G. Kang and X. Wu, *Carbon Capture Sci. Technol.*, 2025, **15**, 100433, DOI: 10.1016/j.ccst.2025.100433.

26 R. Krishna and R. Baur, *Sep. Purif. Technol.*, 2003, **33**, 213–254, DOI: 10.1016/S1383-5866(03)00008-X.

27 X. Hu, M. Yang, D. Fan, G. Qi, J. Wang, J. Wang, T. Yu, W. Li and M. Shen, *J. Catal.*, 2016, **341**, 55–61, DOI: 10.1016/j.jcat.2016.05.022.

28 D. Wang, L. Zhang, J. Li, K. Kamasamudram and W. S. Epling, *Catal. Today*, 2014, **231**, 64–74, DOI: 10.1016/j.cattod.2013.11.040.

29 D. Wang, Z. Li and C. Song, *Mater. Res. Express*, 2021, **8**, 025507, DOI: 10.1088/2053-1591/ABE6D3.

30 M. Zamadics, X. Chen and L. Kevan, *J. Phys. Chem.*, 1992, **96**(6), 2652–2657, DOI: 10.1021/j100185a048.

31 Y. Liu, UCL, University College London, 2021, PhD thesis, https://discovery.ucl.ac.uk/id/eprint/10136256/1/PhD20Thesis_Yiyun20Liu_v2.5.3_submit.pdf.

32 R. Bulánek, B. Wichterlová, Z. Sobalík and J. Tichý, *Appl. Catal. B Environ.*, 2001, **31**, 13–25, DOI: 10.1016/s0926-3373(00)00268-x.

33 J. Y. Lu, Z. Q. Bu, Y. Q. Lei, D. Wang, B. He, J. Wang and W. T. Huang, *J. Mol. Liq.*, 2024, **409**, 125503, DOI: 10.1016/j.molliq.2024.125503.

34 H. Jiang, B. Guan, H. Lin and Z. Huang, *Fuel*, 2019, **254**, 115730, DOI: 10.1016/j.fuel.2019.05.170.

35 C. Niu, X. Shi, F. Liu, K. Liu, L. Xie, Y. You and H. He, *Chem. Eng. J.*, 2016, **298**, 228–235, DOI: 10.1016/j.cej.2016.02.086.
36 X. Wang, M. Qin, Y. Xu and Q. Li, *J. Colloid Interface Sci.*, 2023, **638**, 686–694, DOI: 10.1016/j.jcis.2023.02.023.
37 Y. Ma, Y. Gao, X. Wu, B. Jin, R. Ran, Z. Si and D. Weng, *ACS Appl. Mater. Interfaces*, 2022, **14**, 43442–43455, DOI: 10.1021/acsami.2c13890.